Journal of Magnetism and Magnetic Materials ∎ (∎∎∎∎) ∎∎∎–∎∎∎

Contents lists available at ScienceDirect

Journal of Magnetism and Magnetic Materials

journal homepage: www.elsevier.com/locate/jmmm

Hybrid finite-element/boundary-element method to calculate Oersted fields

Riccardo Hertel [a,*], Attila Kákay [b]

[a] Institut de Physique et Chimie des Matériaux de Strasbourg, Université de Strasbourg, CNRS UMR 7504, Strasbourg, France
[b] Peter Grünberg Institut (PGI-6), Forschungszentrum Jülich GmbH, D-52428 Jülich, Germany

ARTICLE INFO

Article history:
Received 17 October 2013
Received in revised form
3 January 2014

Keywords:
Oersted field
Micromagnetic simulation
Finite element method
Current density distribution

ABSTRACT

The article presents a general-purpose hybrid finite-element/boundary-element method (FEM/BEM) to calculate magnetostatic fields generated by stationary electric currents. The efficacy of this code lies in its ability to simulate Oersted fields in complex geometries with non-uniform current density distributions. As a precursor to the calculation of the Oersted field, an FEM algorithm is employed to calculate the electric current density distribution. The accuracy of the code is confirmed by comparison with analytic results. Two examples show how this method provides important numerical data that can be directly plugged into micromagnetic simulations: The current density distribution in a thin magnetic strip with a notch, and the Oersted field in a three-dimensional contact geometry; similar to the type commonly used in spin-torque driven nano-oscillators. It is argued that a precise calculation of both, the Oersted field and the current density distribution, is essential for a reliable simulation of current-driven micromagnetic processes.

1. Introduction

Over the past 10 years, the study of current-driven magnetization processes has evolved to one of the most active fields in magnetism. Important discoveries demonstrating that, owing to the electron spin, the magnetization state of a nanomagnet could be influenced directly by electrical currents rather than by external magnetic fields [1–4] have led to numerous studies on the spin-transfer torque (STT) effect. The magnetization dynamics induced by STT [5,6] is attractive for both technological aspects and fundamental physics. While field-induced magnetic switching in nanodevices is connected with the technological difficulty to focus magnetic fields on very small length scales, the STT effect provides the possibility to switch, e.g., individual magnetic nanoelements in integrated circuits or in densely packed arrays [7]. Moreover, the current-induced magnetization dynamics differs qualitatively from the field-induced dynamics. An important example thereof is the excitation of high-frequency magnetic oscillations induced by means of DC spin-polarized currents [1,2]; an effect that lacks an analogy in the field-driven dynamics. The possibility to tune the frequency of these oscillations by varying the current strength bears a high potential for applications.

Micromagnetic simulations have nowadays evolved to a very high level of accuracy and reliability, so that they provide essential contributions for the design and for the understanding of functional magnetic nanostructures. While the STT effect has been implemented in several micromagnetic codes [8–10], a quantitative difference between simulated and experimental results is more pronounced in the case of current-induced magnetization dynamics than in standard micromagnetic simulations [11]. Unlike the STT case, numerous studies on the static [12,13] and the field-driven dynamics [14] of nanomagnets have provided a nearly perfect agreement between experiment and simulation.

One of the possible sources for such disagreement is the Oersted field. Current-induced magnetization processes require high current densities, often in the range of 10^{11} A/m^2 . Such current densities are connected with sizable magnetic fields,[1] known as Oersted or Ampère fields [16]. Therefore, in addition to the usual external and internal effective fields entering the Landau–Lifshitz–Gilbert equation [17], and also in addition to the STT term, the Oersted field can have a decisive influence on the magnetization. The importance of the Oersted field in spin-transfer induced magnetic switching process has in fact been pointed out by various groups [18,19]. In view of the aforementioned high accuracy of classical micromagnetic simulations, STT simulations

* Corresponding author. Tel.: +33 38810 7263; fax: +33 38810 7249.
E-mail address: hertel@ipcms.unistra.fr (R. Hertel).

http://dx.doi.org/10.1016/j.jmmm.2014.06.047
0304-8853/

[1] For simplicity we do not consider here some recent developments where pure spin currents without charge transfer have been employed to manipulate nanomagnets [15].

require numerical methods to precisely calculate the Oersted field. In this article a method based on a combination of the finite-element method (FEM) and the boundary element method (BEM) is presented which allows for a fast and accurate calculation of the Oersted field in arbitrary contact geometries. The hybrid FEM/BEM scheme is similar to the algorithm reported by Hrkac et al. [20] and has several advantageous features, including the unproblematic treatment of interactions resulting from Oersted fields in complex nanocircuits [21] or the possibility to simulate arrays containing several current-carrying nanopillars [22].

The article is structured as follows. First, the basic equations and the numerical method for the Oersted field calculation are presented. Subsequently, in Section 5, a method to calculate current-density distributions in non-trivial geometries is outlined. Finally, in Section 6, a few examples show how these methods can be applied to typical geometries employed in studies on current-driven magnetization processes.

2. The ideal symmetric case and its limits

In publications of micromagnetic simulation studies on the current-induced magnetization dynamics it is often mentioned that the Oersted field is included, without providing details on its calculation, cf., e.g., Ref. [23]. This omission of specifications is usually justified, since the calculation of the Oersted field can be trivial when a few plausible assumptions are made. If the current density $\boldsymbol{j}$ is homogeneous and if the current-carrying structure shows no variation along z, where the z axis is the flow direction of the current, the circulation theorem immediately yields the solution. From

$$\nabla \times \boldsymbol{H} = \boldsymbol{j} \tag{1}$$

An integration over a cross-section of the wire parallel to the xy-plane yields

$$\oint \boldsymbol{H}\, \mathrm{d}\boldsymbol{s} = jA \tag{2}$$

where A is the area of the cross-section enclosed by the surface integral, and $d\boldsymbol{s}$ is an infinitesimal tangential line segment along the boundary of A oriented in mathematically positive direction. If the cross-section of the conductor is circular with radius R, one obtains for the boundary

$$H_\phi = jR/2 \tag{3}$$

and $H_\phi(r) = r \cdot j/2$ inside the wire, where $r \le R$ is the distance from the central axis and H_ϕ is the azimuthal component of the Oersted field. It is easy to show that all other magnetic field components are zero. Outside the wire, the field strength decays with $1/r$.

This procedure can be extended, e.g., to elliptical or rectangular cross-sections. In all cases, the Oersted field is zero at the center of the cross-section and its magnitude increases linearly up to its maximum value as it approaches the boundary. The magnetic field lines replicate the shape of the cross-section inside the conductor.

Given the high degree of accuracy that micromagnetic simulations have achieved over the past years, it may however be undesirable to make use of any simplifying assumption, such as translational invariance along z or homogeneous current density distributions $\boldsymbol{j}$. The method described in this article provides an approach to calculate the Oersted field in arbitrary geometries for arbitrary stationary current density distributions.

3. Basic equations

Let us start by considering a current-carrying sample of volume V in which the current density distribution $\boldsymbol{j}(\boldsymbol{r})$ is known for every point $\boldsymbol{r}$. The calculation of $\boldsymbol{j}(\boldsymbol{r})$ will be discussed in Section 5. The Oersted field $\boldsymbol{H}_c$ resulting from a current density distribution $\boldsymbol{j}(\boldsymbol{r})$ can be obtained by direct integration over the volume of the current-carrying particle:

$$\boldsymbol{H}_c(\boldsymbol{r}) = \nabla \times \frac{1}{4\pi} \int \frac{\boldsymbol{j}(\boldsymbol{r}')}{|\boldsymbol{r}-\boldsymbol{r}'|}\, \mathrm{d}V' \tag{4}$$

$$\boldsymbol{H}_c(\boldsymbol{r}) = \int \boldsymbol{j}(\boldsymbol{r}') \times (\nabla' G)\, \mathrm{d}V' \tag{5}$$

where

$$G(\boldsymbol{r}-\boldsymbol{r}') = \frac{1}{4\pi}\frac{1}{|\boldsymbol{r}-\boldsymbol{r}'|} \tag{6}$$

is Green's function with

$$\Delta G = -\delta(\boldsymbol{r}-\boldsymbol{r}') \tag{7}$$

and $\delta(\boldsymbol{r}-\boldsymbol{r}')$ is the Dirac delta function.[2] If the volume of the sample is discretized into finite elements, it is straightforward to implement a routine performing the numerical integration. However, a direct integration according to Eq. (4) is problematic in a numerical sense because of the steep increase of Green's function when $\boldsymbol{r}' \simeq \boldsymbol{r}$. The value of Green's function can in fact vary significantly within a single finite element containing the point $\boldsymbol{r}'$ when the viewpoint $\boldsymbol{r}$ is close to that element. In these cases standard averaging techniques result in an unsatisfactory accuracy. Moreover, the computational effort involved with this direct integration is large: Calculating each component of $\boldsymbol{H}_c$ at a single point $\boldsymbol{r}$ requires an integration over the whole volume V' of the conductor. Instead of integrating directly Eq. (4), it is usually more convenient to solve numerically a set of equivalent partial differential equations. Solving such differential equations is the task of the FEM/BEM formulation outlined in the following.

The fundamental equation for the calculation of the Oersted field is Ampère's law:

$$\nabla \times \boldsymbol{H} = \boldsymbol{j}. \tag{8}$$

In the case of a stationary, current-carrying ferromagnet with magnetization $\boldsymbol{M}$, the magnetostatic field $\boldsymbol{H}$ can be separated in two parts:

$$\boldsymbol{H} = \boldsymbol{H}_s + \boldsymbol{H}_c \tag{9}$$

where $\boldsymbol{H}_s$ is the demagnetizing field (also referred to as dipolar field of stray field in the literature), which is created by the magnetic moments of the ferromagnet. The field $\boldsymbol{H}_c$ is the Oersted field (also called Ampère field) resulting from the current density $\boldsymbol{j}(\boldsymbol{r})$. The following equations apply to these two static magnetic field contributions:

$$\nabla \times \boldsymbol{H}_s = \boldsymbol{0} \quad \nabla \times \boldsymbol{H}_c = \boldsymbol{j} \tag{10}$$

$$\nabla \boldsymbol{H}_s = -\nabla \boldsymbol{M} \quad \nabla \boldsymbol{H}_c = 0 \tag{11}$$

The calculation of $\boldsymbol{H}_s$ is one of the central parts of any micromagnetic code. Several powerful methods have been applied for the numerical calculation of the dipolar field in micromagnetics [24,25]. A very efficient way to calculate the demagnetizing field with finite elements is the hybrid FEM/BEM algorithm reported by Fredkin and Koehler [26]. Even though there are still exciting developments for further improvement of the speed and accuracy in the magnetostatic field calculation of ferromagnets [27], the problem can nowadays considered as solved. Henceforth, only the contribution from the electric current $\boldsymbol{H}_c$ shall be considered, and the subscript "c" is omitted for simplicity.

[2] Note that $\nabla' G = -\nabla G$.

Please cite this article as: R. Hertel, A. Kákay, Journal of Magnetism and Magnetic Materials (2014), http://dx.doi.org/10.1016/j.jmmm.2014.06.047

(Eqs. (10) and 11) yield

$$\Delta \boldsymbol{H} = -\nabla \times \boldsymbol{j}. \tag{12}$$

In the region outside the conductor, the source term is zero, *i.e.*,

$$\Delta \boldsymbol{H} = \boldsymbol{0} \tag{13}$$

Thus, each component of $\boldsymbol{H}$ satisfies the Poisson equation inside the conductor and the Laplace equation outside. (Eqs. (12) and 13) describe an *open boundary problem*. Such problems are characterized by the absence of well-defined boundary conditions at the sample surface. The solution is uniquely defined by the condition of regularity at infinity, *i.e.*, a Dirichlet-type of boundary condition for $r \to \infty$:

$$\lim_{r\to\infty} \boldsymbol{H}(\boldsymbol{r}) = \boldsymbol{0} \tag{14}$$

A possible approach to consider such boundary conditions consists in attempting to expand the computational region to "infinity", *e.g.* by applying bijective transformations to map the infinite volume surrounding the sample onto a volume of finite size, which can then be discretized with finite elements [28]. Such transformation methods can suffer from accuracy problems since the discretized spatial transform effectively corresponds to a truncation of the computational region at a more or less large distance. Moreover, these methods require the external region to be free of charges, thereby precluding the possibility of calculating the field of interacting current carriers. The hybrid finite element/boundary element method resolves these problems. In the boundary element method, the fundamental solution of a partial differential equation is used. In this case, the fundamental solution is given by Green's function, which automatically fulfills the boundary condition at infinity.

4. Hybrid FEM/BEM formulation

The first step in developing the FEM/BEM formulation consists in an analysis of the properties of the solution at the sample boundary. From Eq. (12) a jump condition for the normal derivative of $\boldsymbol{H}_c$ at the boundary of the current carrier is easy to derive:

$$\boldsymbol{n}(\nabla H_x|_{\text{in}} - \nabla H_x|_{\text{out}}) = \boldsymbol{n}(\boldsymbol{e}_x \times \boldsymbol{j}) \tag{15}$$

This equation correspondingly holds also for the y and z components of $\boldsymbol{H}$. In Eq. (15), $\boldsymbol{e}_x$ is the unit vector along the x axis and $\boldsymbol{n}$ is the outward directed surface unit vector. Note that this condition represents a discontinuity of the gradient of H_x at the boundary. Such a discontinuity in the gradient *a priori* does not provide any information on the value of the inward limit of the gradient of H_x. It can therefore not be used as a Neumann boundary condition at the boundary $\partial\Omega$, the knowledge of which would allow for a unique solution of the differential equation.

In order to obtain useful boundary conditions at the sample surface, the Oersted field can be split in two parts, $\boldsymbol{H} = \boldsymbol{H}^{(1)} + \boldsymbol{H}^{(2)}$. These fields shall have the following properties: (i) Outside the current carrier, the part $\boldsymbol{H}^{(1)}$ is zero. (ii) The part $\boldsymbol{H}^{(1)}$ satisfies Poisson's equation

$$\Delta H_x^{(1)} = -\boldsymbol{e}_x \cdot (\nabla \times \boldsymbol{j}) \tag{16}$$

with Neumann boundary conditions

$$\boldsymbol{n}(\nabla H_x^{(1)}|_{\text{in}}) = \boldsymbol{n}(\boldsymbol{e}_x \times \boldsymbol{j}) \tag{17}$$

(iii) The part $\boldsymbol{H}^{(2)}$ satisfies the Laplace equation

$$\Delta H_x^{(2)} = 0 \tag{18}$$

and its derivatives are continuous along the boundary.

The boundary conditions required for the solution of Eq. (18) will be discussed later. The jump condition for the individual components $H^{(1)}$ and $H^{(2)}$ at the boundary

$$H_x^{(1)}|_{\text{in}} + H_x^{(2)}|_{\text{in}} = H_x^{(2)}|_{\text{out}} \tag{19}$$

results from the condition that the field $\boldsymbol{H}$ must be continuous at the surface. The splitting of the field H_x in two parts is schematically shown in Fig. 1. The advantage of this splitting is that it allows to extract boundary conditions that can be used to solve Poisson's equation: By setting $H_x^{(1)}$ to zero outside the sample, the discontinuity condition (15) is effectively converted into a Neumann boundary condition (17). With this boundary condition, it is possible to solve Eq. (16). The finite element method is tailored to provide solutions of equations of the type (16) with given Neumann boundary conditions (17), cf. Ref. [29]. Once this solution is obtained, the somewhat more complicate part needs to be addressed, *i.e.*, finding the values of $\boldsymbol{H}^{(2)}$ at the particle surface. These values will provide the Dirichlet boundary conditions required for the solution of Laplace's equation (18). For this task, the boundary element method is used.

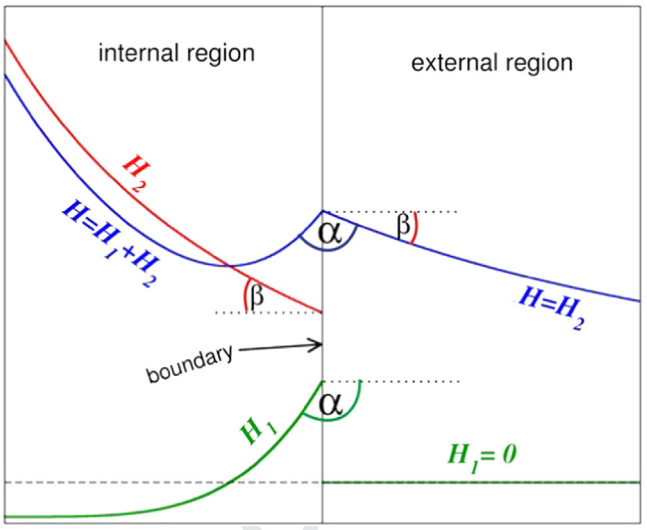

Fig. 1. The field $\boldsymbol{H}$ is split in two parts. The angle α represents the known value of the discontinuity of the derivative of $\boldsymbol{H}$ at the boundary (Eq. 15). The part H_1 of the solution is chosen such that its gradient at the boundary corresponds to α. Moreover, H_1 is equal to zero in the external region. Both, H_1 and H_2 are generally discontinuous at the boundary. The sum, *i.e.*, the field H is however continuous. The gradient of the part H_2 is constant along the boundary, as sketched by the angle β.

Multiplying Eq. (7) with $\boldsymbol{H}_1$ and Eq. (16) with G yields, after subtraction and integration over the volume V of the region Ω:

$$\int G\Delta H_1^x \,\mathrm{d}V' - \int H_1^x \Delta G \,\mathrm{d}V' = \int H_1^x \delta(\boldsymbol{r}-\boldsymbol{r}')\,\mathrm{d}V' - \int \boldsymbol{e}_x(\nabla' \times \boldsymbol{j})G \,\mathrm{d}V' \tag{20}$$

which, by virtue of Green's theorem, transforms into

$$\oint G\frac{\partial H_1^x}{\partial \boldsymbol{n}}\,\mathrm{d}S' - \oint H_1^x \frac{\partial G}{\partial \boldsymbol{n}}\,\mathrm{d}S' = \int H_1^x \delta(\boldsymbol{r}-\boldsymbol{r}')\,\mathrm{d}V' + \oint \boldsymbol{n}(\boldsymbol{e}_x \times \boldsymbol{j})G\,\mathrm{d}S' - \boldsymbol{e}_x \int \boldsymbol{j} \times (\nabla' G)\,\mathrm{d}V'$$

The surface integrals $\oint \mathrm{d}S'$ extend over the boundary $\partial\Omega$ of the region Ω, *i.e.*, the sample surface. If the boundary condition for H_1

$$\frac{\partial H_1^x}{\partial \boldsymbol{n}} = \boldsymbol{n}(\boldsymbol{e}_x \times \boldsymbol{j}) \tag{21}$$

is inserted, the equation simplifies to

$$-\oint H_1^x \frac{\partial G}{\partial \boldsymbol{n}}\,\mathrm{d}S' = \int H_1^x \delta(\boldsymbol{r}-\boldsymbol{r}')\,\mathrm{d}V' - \boldsymbol{e}_x \int \boldsymbol{j} \times (\nabla' G)\,\mathrm{d}V' \tag{22}$$

The last term can be identified as the right-hand side of Eq. (4), yielding

$$-\oint H_1^x \frac{\partial G}{\partial \boldsymbol{n}}\,\mathrm{d}S' = \int H_1^x \delta(\boldsymbol{r}-\boldsymbol{r}')\,\mathrm{d}V' - [H_1^x(\boldsymbol{r}) + H_2^x(\boldsymbol{r})] \tag{23}$$

The integral $\int H_1^x \delta(\boldsymbol{r}-\boldsymbol{r}')\,\mathrm{d}V'$ is trivial as long as the point $\boldsymbol{r}$ is located inside or outside the volume V. The situation requires more attention when $\boldsymbol{r}$ is a point on the surface. In this case, the inward limit is taken by introducing an infinitesimal distance of the point (located in the internal region) to the surface. The resulting integral over the delta function is

$$\int H_1^x \delta(\boldsymbol{r}-\boldsymbol{r}')\,\mathrm{d}V' = \frac{\Psi}{4\pi} H_1^x(\boldsymbol{r}) \tag{24}$$

where Ψ is the solid angle subtended at the boundary point $\boldsymbol{r}$.

Hence, an equation is obtained with which $H_2^x(\boldsymbol{r})$ can be calculated at each boundary point:

$$H_2^x(\boldsymbol{r}) = \oint H_1^x(\boldsymbol{r}') \frac{\partial G}{\partial \boldsymbol{n}}\,\mathrm{d}S' + \left(\frac{\Psi}{4\pi} - 1\right) H_1^x(\boldsymbol{r}) \tag{25}$$

Accurate numerical methods to perform this integral by means of BEM are discussed in Ref. [30]. In principle, Eq. (23) would be sufficient to calculate $\boldsymbol{H}_2$ at any point inside (and outside) the volume, so that the resulting total field $\boldsymbol{H} = \boldsymbol{H}_1 + \boldsymbol{H}_2$ could be calculated at any discretization point. However, the calculation of $\boldsymbol{H}_2$ at one point $\boldsymbol{r}$ requires in this case an integration over the whole surface. This approach would thus have similar disadvantages as the direct integration according to Eq. (4). By using Eq. (25) instead, we obtain at relatively low cost the boundary values of $\boldsymbol{H}_2$. Having these Dirichlet boundary conditions, it is easy to solve Eq. (18) in the volume V by means of the FEM.

It is noteworthy that Eq. (25) has the same form as it has been used in the FEM/BEM scheme described in Ref. [26] to calculate the scalar magnetic potential of a ferromagnet. From the viewpoint of implementation into a program, this means that the matrix required for the numerical calculation the values of $\boldsymbol{H}_2$ according to Eq. (25) is already available in the micromagnetic code if the FEM/BEM scheme presented in Ref. [26] is used for the calculation of the magnetic scalar potential. Moreover, the matrix has the usual form of BEM schemes for which powerful matrix compression schemes [31] have been developed that can help reducing drastically the memory requirements.

5. Calculation of current density distributions

Unless the geometry of the current-carrying sample is trivial, the current density distribution $\boldsymbol{j}(\boldsymbol{r})$ needs to be determined numerically prior to the calculation of the Oersted field. The starting point for the calculation of the current density distribution is Ohm's law

$$\boldsymbol{j} = \sigma \boldsymbol{E}, \tag{26}$$

where $\boldsymbol{E}$ is the local electric field and the conductivity σ is assumed to be a scalar. The electric field is the gradient field of the electrostatic potential U, so that $\boldsymbol{E} = -\nabla U$. Charge conservation yields $\nabla \boldsymbol{E} = 0$ and thus $\nabla \boldsymbol{j} = 0$, which leads to

$$\nabla(\sigma \nabla U) = 0 \tag{27}$$

This equation has the form of the stationary diffusion equation and converts into the Laplace equation for U if σ is homogeneous.

Elliptic differential equations of the type (27) are routinely solved numerically with FEM. However, appropriate boundary conditions must be specified to obtain a unique solution. In this case, the boundary conditions are given by the fact that the current is not flowing perpendicular to the sample surface $\boldsymbol{j} \cdot \boldsymbol{n} = 0$; except for the leads, where a known current density is entering and leaving the sample. In the case of two contact leads of the same size, the boundary condition is $\boldsymbol{j} \cdot \boldsymbol{n} = \pm j_0$ at the leads, *i.e.*,

$$\frac{\partial U}{\partial n} = \begin{cases} \mp j_0/\sigma & \text{at the leads} \\ 0 & \text{at the rest of the boundary} \end{cases} \tag{28}$$

If only the value of the total current I flowing through the sample is known, the current density at the positive and negative leads is easily determined by dividing the total current flowing through each lead by the area of the contact region. Obviously, care must be taken that the total inflowing current is equal to the outflowing. Note that with correct Neumann boundary conditions, Eq. (27) can be solved without further changes also in the more general case of a position-dependent conductivity $\sigma(\boldsymbol{r})$.

The method described here for the calculation of current density distributions is generally well known [32–34]. It is included in this manuscript mainly for completeness, because determining the current density distribution is usually a prerequisite for the calculation of the Oersted field.

6. Examples

The methods outlined above can be applied to various problems which are of high importance for modern research topics in the field of nanomagnetism. In this section, a few examples are presented. These include the current density distribution in a thin strip with an notch and the calculation of the current density distribution and of the Oersted field in a pillar contact geometry as it is used to study high-frequency excitations in nanomagnets [1,35].

6.1. Current density distribution in a thin strip with a notch

Ferromagnetic thin strips with width in the sub-μm range and thicknesses of the order of a few ten nm have attracted much interest over the past years. One reason is the particular type of head-to-head domain walls that can develop in such structures [36]. Magnetic strips have been proposed for nanomagnetic devices in which the head-to-head domain walls represent units of information that can be processed in logical devices [37,38]. It has further been shown that the domain walls in such strips can be displaced by means of the STT effect [3,4]. Since the domain walls can be displaced continuously along a magnetic strip, it is of practical importance to gain control of their position. This can be achieved by means of notches in the strips, which act as an attractive potential for the domain walls [39]. Depending on their type, the domain walls are then either located exactly at the notch or in its close vicinity [40,39].

The influence of notches on the micromagnetic configuration has been studied intensively and reported in several publications. However, notches do not only affect the micromagnetic structure but also change the current density distribution within the strip. This aspect is important for the study of current-driven domain wall dynamics in such patterned strips.

Using the method described in the previous section, it is straightforward to determine the current density distribution with finite element simulations. The model used in this example is a 1.2 μm long strip (width: 100 nm, thickness: 20 nm) with a notch in the center. The notch has the shape of a symmetric right triangle and it reduces the width of the strip to 50 nm in the narrowest part. The region of interest of the finite element mesh is shown in the inset of Fig. 2. In the vicinity of the notch, the tetrahedral mesh is locally refined to increase the numerical accuracy. A total current of $I = 2$ mA is flowing along the wire, and a homogeneous electric conductivity is assumed.

Please cite this article as: R. Hertel, A. Kákay, Journal of Magnetism and Magnetic Materials (2014), http://dx.doi.org/10.1016/j.jmmm.2014.06.047

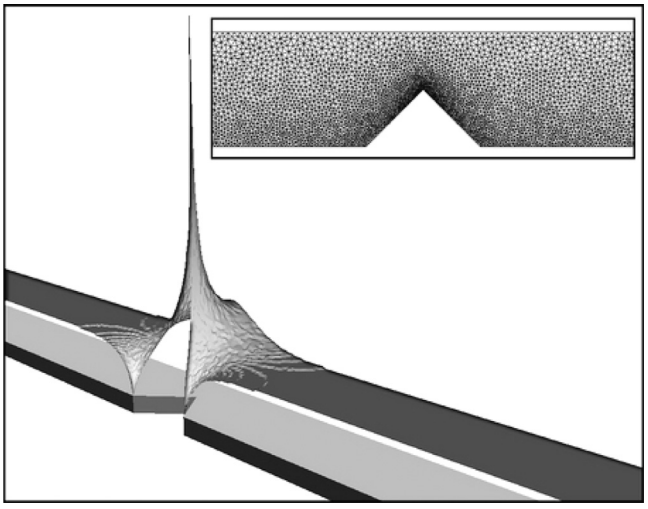

Fig. 2. Current density distribution in a thin, flat strip with a notch. The inset shows a part of the finite-element mesh used for the analysis close to the constriction. The main image shows a perspective view on the region of interest near the notch and a topographical representation of the magnitude of the local current density. The strip is contacted such that the current flows parallel to the strip. The local current density increases dramatically near the apex of the notch. Contrary to this, the current density on the flat side of the constriction is only slightly higher than the value in the unconstrained parts of the strip.

The topographical representation in Fig. 2 displays the local value of the current density. As expected, the current density increases at the constriction. The Much impact of the notch is however much more important than the reduction of the width. Where the wire is not constrained, the current density is $j = 10^{12}$ A/m^2. At the apex of the notch, the value increases drastically to $j = 5.5 \times 10^{12}$ A/m^2, while in the opposite, flat part of the strip it only increases up to $j = 1.55 \times 10^{12}$ A/m^2. Hence, in the narrow part of the strip, the current density distribution is highly inhomogeneous. Over the small distance of 50 nm it changes almost by a factor of four. The values of the local current density obviously scale linearly with the applied current. The value of 2 mA has only been chosen here as an example since the resulting current density values are of the order of those reported in corresponding experimental studies. The current density *profile* is independent of the value of the applied current. Hence, the inhomogeneities of the current density distribution are directly connected with the sample geometry, and not with the value of the applied current. The profile is moreover invariant with respect to scaling. For completeness, it should be pointed out that singularities like the one displayed here are well-known effects in the case of laminar flow of incompressible liquids. Even though the current density in reality never becomes singular, an accurate simulation of these critical situations is a difficult and important task.

This drastically inhomogeneous current density distribution near a notch can be very important for the design and for the understanding of devices based on current-driven domain-wall displacement. The huge differences of the local current density in the constriction region could have a strong impact on the STT effect, electromigration processes, and on the heating of the sample.

6.2. Oersted field calculation – comparison with analytics

The method presented in Section 4 to calculate the Oersted field for a given current density distribution can be tested by comparing the numerical results with known analytic solutions. A simple example is the magnetic field of an infinitely long current-carrying cylinder with homogeneous current density. The current is flowing parallel to the symmetry axis. If a wire with radius R is parallel to the z direction, with the current I flowing along $\boldsymbol{e}_z$ and ϕ

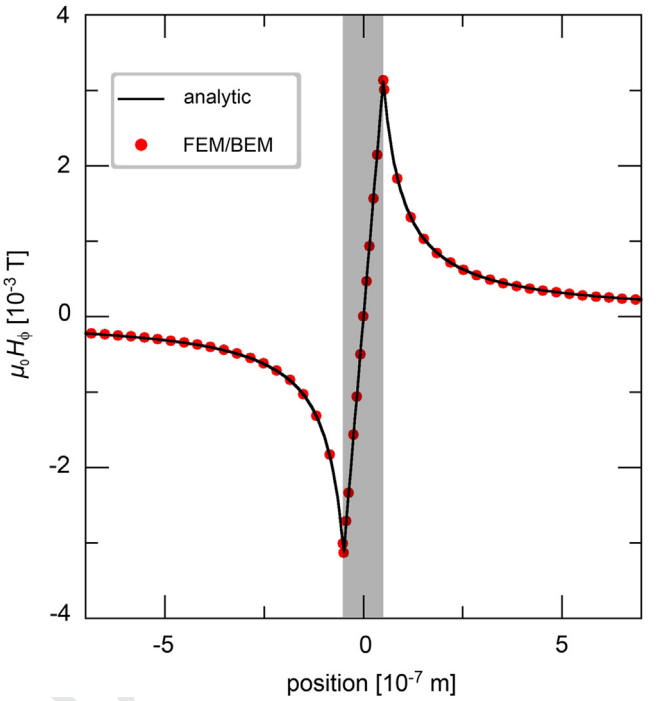

Fig. 3. Oersted field of a long, current-carrying cylinder with homogeneous current density. The current is flowing parallel to the wire axis. In this case, the field $\boldsymbol{H}$ only has an azimuthal component. The computed values (dots) perfectly match with the analytic solution (line). The grey area denotes the region inside the wire.

and ρ being the azimuthal and radial coordinate, respectively, the Oersted field is

$$\boldsymbol{B}(\boldsymbol{r}) = \mu_0 H(\rho)\boldsymbol{e}_\phi = \frac{\mu_0 I}{2\pi}\boldsymbol{e}_\phi \begin{cases} \rho/R^2 & (\rho \le R) \\ 1/\rho & (\rho > R) \end{cases} \tag{29}$$

In Fig. 3 this analytical result (solid line) is compared with the computed values (dots) resulting from the FEM/BEM simulation in the case of an 8 μm long wire with $R = 50$ nm and homogeneous current density $\boldsymbol{j} = 10^{11}$ A/m$^2 \cdot \boldsymbol{e}_z$. Excellent agreement is obtained. Numerical tests show that minor deviations can be further reduced by increasing the discretization density, but are not of practical importance. This example proves the correctness and accuracy of the hybrid FEM/BEM scheme. Obviously, the advantage of the FEM/BEM algorithm is its applicability to samples of complex shape, which cannot be calculated analytically. Such an example is given in the following subsection, where the current density distribution and the resulting Oersted field are calculated for a complex contact geometry as it is used to study current-induced stationary high-frequency excitations of nanomagnets.

6.3. Current densities and Oersted fields in a nanopillar contact geometry

The possibility of generating high-frequency, stationary oscillations in a nanomagnet with a DC current has attracted much attention over the past years. This effect can occur when a submicron sized ferromagnetic thin-film element is exposed to a spin-polarized current flowing perpendicularly through its surface. It was predicted [5,6] theoretically and a few later confirmed experimentally [1]. In experimental setups on such spin-torque driven nano-oscillators, the thin-film element is typically embedded into a pillar-shaped multilayer structure, which is contacted by mesoscopic leads on the top and on the bottom. The electric current flows parallel to the pillar axis. Numerous experimental and numerical studies on the current-induced magnetization dynamics in nanomagnets within

Please cite this article as: R. Hertel, A. Kákay, Journal of Magnetism and Magnetic Materials (2014), http://dx.doi.org/10.1016/j.jmmm.2014.06.047

a pillar contact have been reported (see, e.g., [41] and references therein) and the field remains very active. While the STT effect is driving the magnetization dynamics, the Oersted field connected with the electric current may represent a non-negligible perturbation which could have an important impact on the magnetization dynamics. Considering that, also in this case, typical current densities are of the order of 10^{12} A/m^2, the Oersted field can provide a sizable contribution even when the pillar dimensions are deep in the sub-micron range.

The Oersted field in such complicated contact geometries can be obtained by first calculating the current density distribution and, based on this, determining the magnetic field using the method described before. In addition to the current flowing through the pillar, also the current in the leads contributes to the total magnetic field acting on the nanomagnet. Fig. 4 shows the finite-element mesh used to simulate the current and field distribution in a pillar contact geometry. In this example, the pillar diameter is 50 nm and the pillar height is 120 nm. It is contacted by strips of 500 nm width and 100 nm thickness. Each contacting strip is 4 μm long and the top and bottom electrodes form an angle of 90°. The geometry roughly corresponds to the usual experimental setups [35], even though the contacting strips are often much wider than those used here. By defining the FEM mesh, the details of the shape of the contacts can easily be adapted to any experimental setup.

In this example, a current of 2 mA flows through the sample. The current density inside the pillar is according to the above-mentioned diameter $j \simeq 10^{12}$ A/m^2. At sufficiently large distance from the pillar, the current density in the contacting strip is nearly homogeneous $j = 4 \times 10^{10}$ A/m^2. A complicated situation develops in the vicinity of the contact to the pillar. The non-trivial current density distribution in this region is shown in Fig. 5.

Once the discretized form of the vector field $\boldsymbol{j}(\boldsymbol{r})$ is calculated, it can be used as an input for the Oersted field calculation. By applying the FEM/BEM algorithm we obtain the Oersted field in the entire contact geometry, including the pillar. The result is displayed in Fig. 6, where the field circulation around the contacting strips and around the pillar can clearly be seen. For clarity, only the field in the contacting strips is displayed.

For such experiments and the correct interpretation of the data, the field distribution inside the pillar can play a decisive role. The profile of the field inside the pillar is very similar to the one displayed in Fig. 3: The dominant component of the field is azimuthal, with a magnitude that inside the pillar increases linearly with the distance from the central axis. The peak value at the boundary of the pillar is in this case 28 mT, which certainly represents a non-negligible magnitude. Compared with the field strength due to the current flowing in the pillar, the field arising from the current in the contacting strips can be considered as a perturbation. This perturbation provides in this case merely an asymmetry along a direction at 45° with respect to the strips. Due to this asymmetry, the magnitude of the maximum and the minimum value of both, the x and the y components of the Oersted field differ by about 12%. Whether this asymmetry is essential depends on the specific experimental setup and the problem that is being investigated.

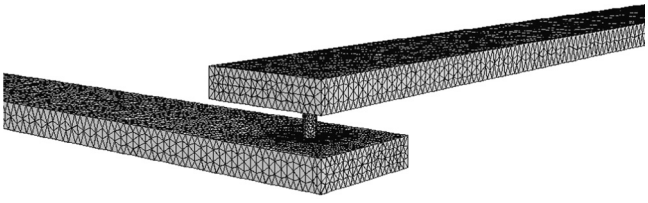

Fig. 4. Perspective view on the finite-element mesh used for the contact geometry. The ends of the 4 μm long contacting strips, where the current is flowing into and out of the sample, are located outside of this frame, which is a magnified view on the region of interest where the pillar is located. The mesh is locally refined at the nanopillar.

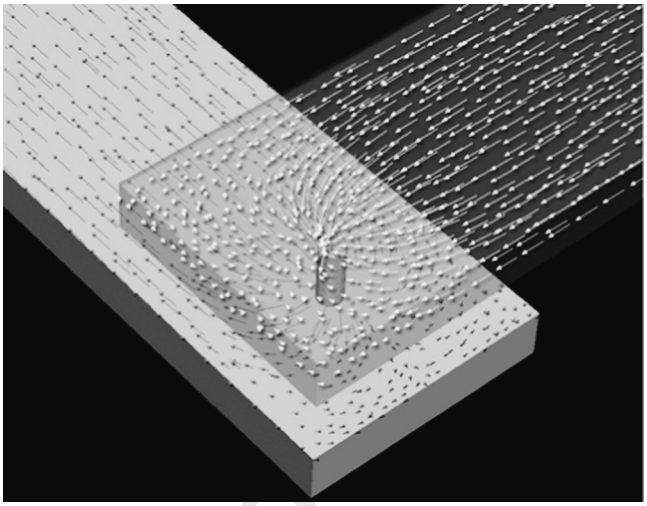

Fig. 5. Simulated current density distribution in the contact geometry. The arrows represent the direction of the local current, and their length is proportional to the local value of the current density. For better visibility, only a selection of the computed data is shown. For the same reason, the current density distribution inside the pillar is not shown, since the much larger current density there would result in very long arrows in this representation. The top electrode is displayed as semi-transparent in order to visualize the current density distribution inside the leads.

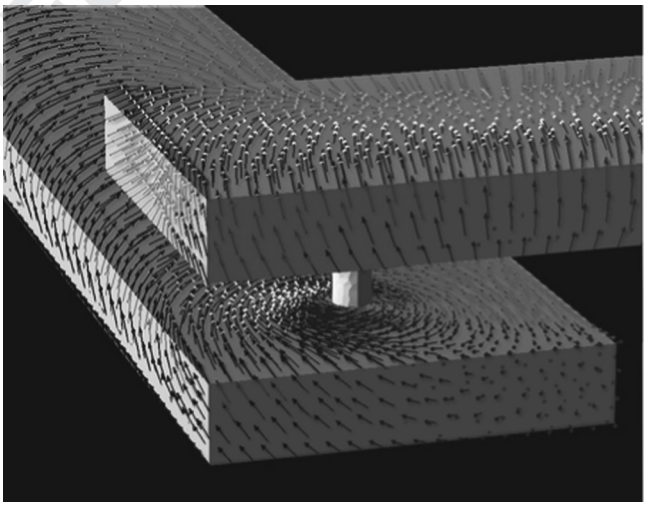

Fig. 6. Computed Oersted field resulting from the current distribution shown in Fig. 5. The circulation of the magnetic field around the current-carrying regions is clearly visible. The black arrows have a component directed outside of the sample, while the pale gray arrows are pointing towards the inside. Only the magnetic field at the surfaces of the leads is displayed. The magnetic field of the pillar is not shown for better visibility of the overall structure of the field.

6.4. Impact of the Oersted field on a spin-torque-driven nano-oscillator

It was mentioned at the beginning that Oersted fields may also play an important role in the case of spin-transfer-torque driven nano-oscillators [1]. Such oscillators consist of a “free” magnetic layer that is usually a soft-magnetic thin-film element of circular or elliptical shape, with a typical size of about 100 nm. This thin-film element is embedded into a layered pillar structure, where a “fixed” layer acts as a spin polarizer. The fixed layer usually has a larger thickness than and a pronounced in-plane anisotropy. The

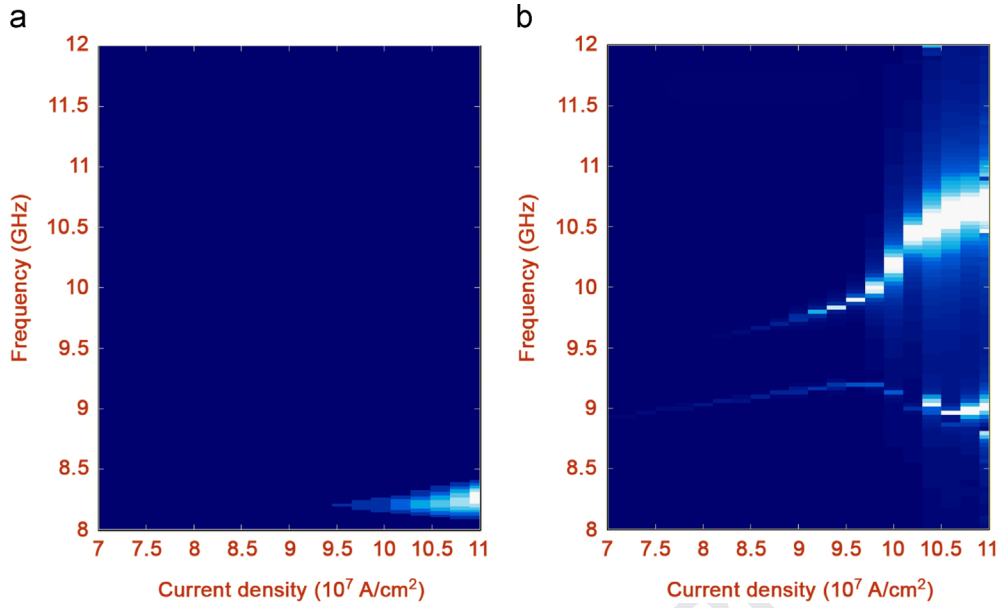

Fig. 7. (a) Oscillations of the magnetization in a spin-torque driven nano-oscillator (see text) as a function of the applied current. The data is obtained from micromagnetic simulations in which only the spin-transfer-torque effect and the usual Landau–Lifshitz dynamics is taken into account. The color code displays the intensity of the oscillation at a specific frequency. The data is obtained from a detailed Fourier analysis of the oscillations of the nanoplatelet performed over several tens on nanoseconds. (b) Oscillations of the magnetization in the same nanopillar when the Oersted field connected with the current flowing through the nanopillar is included in the simulations. The fundamental mode [the same mode as in panel a)] exhibits a shift to higher frequencies (blue-shift) when excited with current densities above 8×10^7 A/cm^2. (For interpretation of the references to color in this figure caption, the reader is referred to the web version of this paper.)

free and the fixed layer are separated by a thin non-magnetic layer and the current flows along the pillar, *i.e.*, perpendicular to the surface of the free layer. The quotation marks in the words "free" and "fixed" have been used because these terms represent idealizations, since the polarizer also experiences a spin-torque due to back-scattered polarized electrons and the free layer may encounter various energetic obstacles in its motion.

Micromagnetic simulations with spin-transfer-torque dynamics allow to investigate a situation that is not realistic in an experiment, where a strong current density flows through the pillar without generating any Oersted field. Such simulations are useful to identify the impact of the Oersted field on the overall dynamics, by comparing the result with the data obtained if the Oersted field is correctly included.

Fig. 7 displays an example of such a comparison. When a sufficiently strong DC current flows through the pillar, it excites persistent oscillations in the free layer. In this case the free layer is an epitaxial Fe disk of 2 nm thickness and 150 nm diameter. An in-plane external field of 100 mT is applied along the hard axis (110) of the Fe disk. A current with spin-polarization opposite to the direction of the magnetization is flowing homogeneously, perpendicular through the surface of the disk. Typical material parameters for Fe with cubic anisotropy are used in the simulation. The spin-polarization is set to 30% and the Gilbert damping α is equal to 0.01. A detailed description of the fine-splitting and the additional modes occurring in the free layer because of the Oersted field would go beyond the scope of this article. The results shown in Fig. 7 are only meant as an example to show that, in a typical setup of a spin-torque nano-oscillator, the Oersted field can influence the oscillation spectrum decisively, introducing quantitative and qualitative changes compared to the hypothetical case of an Oersted-field free spin-polarized current.

7. Artifacts due to the truncation

The FEM/BEM algorithm to calculate Oersted described in this article relies on a given current density distribution $\boldsymbol{j}(\boldsymbol{r})$. For practical reasons the current is assumed to enter at one part of the circuit and exit at another. In these regions where the current enters and exits the conductor, it displays a discontinuity, since the current density jumps from zero (outside the surface) to a constant finite value within the conductor. This sudden appearance of the current does not represent a real physical situation. It can be shown that, in the algorithm described above, this discontinuity of the current density at the end of the contacting leads has the same effect as a magnetic surface charge distribution. These purely artificial surface charges create a spurious magnetic field. Owing to the rapid decay of this field, the effect is negligible at reasonable distance from the points of entry and exit of the current. The vague expression "reasonable distance" cannot be quantified in absolute terms since it depends on each individual case, *i.e.*, the geometry of the structure and the contacting leads. Moreover, the problem is invariant with respect to scaling. Therefore, a distance can only be defined as large by comparison with the region of interest, e.g., the size of a nanomagnet in a pillar geometry. The effect of spurious magnetic fields is comparable to the case of a homogeneously magnetized long wire with the magnetization along the symmetry axis. The ends of the wires are positive and negative poles of the field $\boldsymbol{H}$, but the magnetostatic field is quickly diluted geometrically and can be neglected at distances $l \gg r$ from the wire end, if r is the wire radius.

8. Conclusion

The classical interaction of electric currents with the magnetization of ferromagnets is given by the Oersted field. Its importance should not be underestimated in theoretical studies in the highly active field of spin-transfer-torque driven magnetization processes. The Oersted field obtained in the case of typical experimental contact geometries can be as large as a few tens of mT. The STT-driven dynamics of nanomagnets could be influenced significantly by such strong Oersted field. The hybrid FEM/BEM method

Please cite this article as: R. Hertel, A. Kákay, Journal of Magnetism and Magnetic Materials (2014), http://dx.doi.org/10.1016/j.jmmm.2014.06.047

presented in this article provides a flexible and accurate tool to calculate the Oersted field in arbitrary geometries for any given stationary current density distribution.

Also in the case of current-induced domain wall displacement in ferromagnetic strips, inhomogeneities of the current density distribution and/or the magnetostatic field should be considered in micromagnetic simulations if the cross-section of the domain wall is not constant. Notches, often used to capture moving domain walls, can have a dramatic impact on the current-density distribution in thin strips. In these cases, the drastic local increase of the current density should be considered in the simulation of STT-driven domain wall motion.

Acknowledgments

R.H. is indebted to Dr. Alexey V. Khvalkovskiy for several fruitful discussions, and thanks Prof. Claus M. Schneider for valuable comments on the manuscript. R.H. also wishes to thank Dr. Sebastian Gliga for his precious help on the graphical representation of the computed field and current distributions.

References

[1] S.I. Kiselev, J.C. Sankey, I.N. Krivorotov, N.C. Emley, R.J. Schoelkopf, R.A. Buhrman, D.C. Ralph, Microwave oscillations of a nanomagnet driven by a spin-polarized current, Nature 425 (6956) (2003) 380–383.

[2] W. Rippard, M. Pufall, S. Kaka, S. Russek, T. Silva, Direct-current induced dynamics in Co90Fe10/Ni80Fe20 point contacts, Phys. Rev. Lett. 92 (2).

[3] M. Tsoi, R.E. Fontana, S.S.P. Parkin, Magnetic domain wall motion triggered by an electric current, Appl. Phys. Lett. 83 (13) (2003) 2617.

[4] N. Vernier, D.A. Allwood, D. Atkinson, M.D. Cooke, R.P. Cowburn, Domain wall propagation in magnetic nanowires by spin-polarized current injection, Europhys. Lett. (EPL) 65 (4) (2004) 526.

[5] J.C. Slonczewski, Current-driven excitation of magnetic multilayers, J. Magn. Magn. Mater. 159 (1–2) (1996) L1–L7.

[6] L. Berger, Emission of spin waves by a magnetic multilayer traversed by a current, Phys. Rev. B 54 (13) (1996) 9353–9358.

[7] Y. Liu, S. Gliga, R. Hertel, C.M. Schneider, Current-induced magnetic vortex core switching in a permalloy nanodisk, Appl. Phys. Lett. 91 (2007) 112501.

[8] D.V. Berkov, N.L. Gorn, Micromagnetic simulations of the magnetization precession induced by a spin-polarized current in a point-contact geometry (invited), J. Appl. Phys. 99 (8) (2006) 08Q701.

[9] E. Martinez, L. Torres, L. Lopez-Diaz, M. Carpentieri, G. Finocchio, Spin-polarized current-driven switching in permalloy nanostructures, J. Appl. Phys. 97 (10) (2005) 10E302.

[10] K.-J. Lee, A. Deac, O. Redon, J.-P. Nozieres, B. Dieny, Excitations of incoherent spin-waves due to spin-transfer torque, Nat. Mater. 3 (12) (2004) 877–881.

[11] D. Berkov, J. Miltat, Spin-torque driven magnetization dynamics: micromagnetic modeling, J. Magn. Magn. Mater. 320 (7) (2008) 1238–1259.

[12] S. Cherifi, R. Hertel, J. Kirschner, H. Wang, R. Belkhou, A. Locatelli, S. Heun, A. Pavlovska, E. Bauer, Virgin domain structures in mesoscopic co patterns: comparison between simulation and experiment, J. Appl. Phys. 98 (2005) 043901.

[13] R. Hertel, O. Fruchart, S. Cherifi, P.-O. Jubert, S. Heun, A. Locatelli, J. Kirschner, Three-dimensional magnetic-flux-closure patterns in mesoscopic Fe islands, Phys. Rev. B 72.

[14] M. Buess, R. Höllinger, T. Haug, K. Perzlmaier, U. Krey, D. Pescia, M.R. Scheinfein, D. Weiss, C.H. Back, Fourier transform imaging of spin vortex eigenmodes, Phys. Rev. Lett. 93 (7) (2004) 077207.

[15] T. Yang, T. Kimura, Y. Otani, Giant spin-accumulation signal and pure spin-current-induced reversible magnetization switching, Nat. Phys. 4 (11) (2008) 851–854.

[16] J.D. Jackson, Classical Electrodynamics, third edition, Wiley, 1999.

[17] T.L. Gilbert, A phenomenological theory of damping in ferromagnetic materials, IEEE Trans. Magn. 40 (6) (2004) 3443–3449.

[18] Y. Acremann, J. Strachan, V. Chembrolu, S. Andrews, T. Tyliszczak, J. Katine, M. Carey, B. Clemens, H. Siegmann, J. Stöhr, Time-resolved imaging of spin transfer switching: beyond the macrospin concept, Phys. Rev. Lett. 96 (21).

[19] K. Ito, T. Devolder, C. Chappert, M. Carey, J. Katine, Micromagnetic simulation on effect of oersted field and hard axis field in spin transfer torque switching, J. Phys. D.: Appl. Phys. 40 (2007) 1261.

[20] G. Hrkac, T. Schrefl, O. Ertl, D. Suess, M. Kirschner, F. Dorfbauer, J. Fidler, Influence of eddy current on magnetization processes in submicrometer permalloy structures, IEEE Trans. Magn. 41 (10) (2005) 3097–3099.

[21] S.S. P. Parkin, United States Patent: 6834005 – Shiftable Magnetic Shift Register and Method of Using the Same, Dec. 2004.

[22] S. Kaka, M.R. Pufall, W.H. Rippard, T.J. Silva, S.E. Russek, J.A. Katine, Mutual phase-locking of microwave spin torque nano-oscillators, Nature 437 (7057) (2005) 389–392.

[23] I.N. Krivorotov, D.V. Berkov, N.L. Gorn, N.C. Emley, J.C. Sankey, D.C. Ralph, R.A. Buhrman, Large-amplitude coherent spin waves excited by spin-polarized current in nanoscale spin valves, Phys. Rev. B 76 (2) (2007) 024418.

[24] Q. Chen, A. Konrad, A review of finite element open boundary techniques for static and quasi-static electromagnetic field problems, IEEE Trans. Magn. 33 (1) (1997) 663–676.

[25] S.W. Yuan, H.N. Bertram, Fast adaptive algorithms for micromagnetics, IEEE Trans. Magn. 28 (5) (1992) 2031–2036.

[26] D.R. Fredkin, T.R. Koehler, Hybrid method for computing demagnetizing fields, IEEE Trans. Magn. 26 (2) (1990) 415–417.

[27] A. Goncharov, G. Hrkac, J. Dean, T. Schrefl, Kronecker product approximation of demagnetizing tensors for micromagnetics, J. Comput. Phys. 229 (7) (2010) 2544–2549.

[28] X. Brunotte, G. Meunier, J.F. Imhoff, Finite element modeling of unbounded problems using transformations: a rigorous, powerful and easy solution, IEEE Trans. Magn. 28 (2) (1992) 1663–1666.

[29] O.C. Zienkiewicz, R.L. Taylor, J.Z. Zhu, The Finite Element Method Its Basis and Fundamentals, sixth edition, Elsevier, 2005.

[30] D. Lindholm, Three-dimensional magnetostatic fields from point-matched integral equations with linearly varying scalar sources, IEEE Trans. Magn. 20 (5) (1984) 2025–2032.

[31] S. Börm, L. Grasedyck, Hierarchical Matrices, URL: ⟨http://www.hlib.org/literature.html⟩.

[32] J. Moussa, L. Ram-Mohan, J. Sullivan, T. Zhou, D. Hines, S. Solin, Finite-element modeling of extraordinary magnetoresistance in thin film semiconductors with metallic inclusions, Phys. Rev. B 64 (18).

[33] M. Holz, O. Kronenwerth, D. Grundler, Magnetoresistance of semiconductor-metal hybrid structures: the effects of material parameters and contact resistance, Phys. Rev. B 67 (19).

[34] G. Sarau, S. Gliga, R. Hertel, C.M. Schneider, Magnetization reversal of micron-scale cobalt structures with a nanoconstriction, IEEE Trans. Magn. 43 (2007) 2854–2856.

[35] H. Dassow, R. Lehndorff, D.E. Bürgler, M. Buchmeier, P.A. Grünberg, C.M. Schneider, A. van der Hart, Normal and inverse current-induced magnetization switching in a single nanopillar, Appl. Phys. Lett. 89 (22) (2006) 222511.

[36] R.D. McMichael, M.J. Donahue, Head to head domain wall structures in thin magnetic strips, IEEE Trans. Magn. 33 (5) (1997) 4167–4169.

[37] R. Moriya, L. Thomas, M. Hayashi, Y.B. Bazaliy, C. Rettner, S.S.P. Parkin, Probing vortex-core dynamics using current-induced resonant excitation of a trapped domain wall, Nat. Phys. 4 (5) (2008) 368–372.

[38] D.A. Allwood, G. Xiong, M.D. Cooke, C.C. Faulkner, D. Atkinson, N. Vernier, R.P. Cowburn, Submicrometer ferromagnetic NOT gate and shift register, Science 296 (5575) (2002) 2003–2006.

[39] M. Kläui, C. Vaz, W. Wernsdorfer, E. Bauer, S. Cherifi, S. Heun, A. Locatelli, G. Faini, E. Cambril, L. Heyderman, J. Bland, Domain wall behaviour at constrictions in ferromagnetic ring structures, Phys. B: Condens. Matter 343 (14) (2004) 343–349.

[40] R. Moriya, L. Thomas, M. Hayashi, Y.B. Bazaliy, C. Rettner, S.S.P. Parkin, Probing vortex-core dynamics using current-induced resonant excitation of a trapped domain wall, Nat. Phys. 4 (5) (2008) 368–372.

[41] M.D. Stiles, J. Miltat, Spin-transfer torque and dynamics, in: B. Hillebrands, A. Thiaville (Eds.), Spin Dynamics in Confined Magnetic Structures III, No. 101 in Topics in Applied Physics, Springer, Berlin, Heidelberg, 2006, pp. 225–308.

Please cite this article as: R. Hertel, A. Kákay, Journal of Magnetism and Magnetic Materials (2014), http://dx.doi.org/10.1016/j.jmmm.2014.06.047